Monthly Notices of the ROYAL ASTRONOMICAL SOCIETY

MNRAS **448,** 2384–2396 (2015) doi:10.1093/mnras/stv155

CMB distortion from circumgalactic gas

Priyanka Singh,[1]★ Biman B. Nath,[1] Subhabrata Majumdar[2] and Joseph Silk[3,4]

[1]*Raman Research Institute, Sadashivanagar, Bangalore 560080, India*
[2]*Tata Institute of Fundamental Research, Mumbai 400005, India*
[3]*Institut d'Astrophysique, 75014 Paris, France*
[4]*The John Hopkins University, Baltimore, MD 20218, USA*

Accepted 2015 January 20. Received 2014 December 4; in original form 2014 August 20

ABSTRACT

We study the Sunyaev–Zel'dovich (SZ) distortion of the cosmic microwave background radiation from extensive circumgalactic gas (CGM) in massive galactic haloes. Recent observations have shown that galactic haloes contain a large amount of X-ray emitting gas at the virial temperature, as well as a significant amount of warm O VI absorbing gas. We consider the SZ distortion from the hot gas in those galactic haloes in which the gas cooling time is longer than the halo destruction time-scale. We show that the SZ distortion signal from the hot gas in these galactic haloes at redshifts $z \approx 1$–8 can be significant at small angular scales ($\ell \sim 10^4$), and dominate over the signal from galaxy clusters. The estimated SZ signal for most massive galaxies (halo mass $\geq 10^{12.5}$ $M_\odot$) is consistent with the marginal detection by *Planck* at these mass scales. We also consider the SZ effect from warm circumgalactic gas. The integrated Compton distortion from the warm O VI absorbing gas is estimated to be $y \sim 10^{-8}$, which could potentially be detected by experiments planned for the near future. Finally, we study the detectability of the SZ signal from circumgalactic gas in two types of surveys, a simple extension of the South Pole Telescope survey and a more futuristic cosmic-variance-limited survey. We find that these surveys can easily detect the kinetic Sunyaev–Zel'dovich signal from CGM. With the help of a Fisher matrix analysis, we find that it will be possible for these surveys to constrain the gas fraction in CGM, after marginalizing over cosmological parameters, to ≤ 33 per cent, in case of no redshift evolution of the gas fraction.

Key words: galaxies: evolution – galaxies: haloes – cosmic background radiation.

1 INTRODUCTION

The standard scenario of galaxy formation predicts that baryonic gas falls into dark matter potentials and gets heated to the virial temperature (Silk 1977; White & Rees 1978; White & Frenk 1991). This gas then cools radiatively, and if the temperature is low enough ($T \leq 10^6$ K) for significant radiation loss, then most of the galactic halo gas drops to low temperature and no accretion shock develops in the halo (Birnboim & Dekel 2003). In the case of low-mass galaxies, most of the accretion takes place through the infall of cold material from the intergalactic medium (IGM). However, in massive galaxies, the hot halo gas cools slowly and should remain warm/hot for a considerable period of time. This halo gas, if present, could potentially contain a large fraction of the baryons in the Universe which is unaccounted for by collapsed gas and stars in galaxies, and could explain the missing baryon problem (Fukugita, Hogan & Peebles 1998; Anderson & Bregman 2010).

Although numerical simulations have shown that disc galaxies should be embedded in a hot gaseous halo, this gas has been difficult to nail down observationally because of faintness of the X-ray emission (Benson et al. 2000; Rassmussen et al. 2009; Crain et al. 2010). Recent observations have finally discovered this hot coronal gas extended over a large region around massive spiral galaxies (Anderson & Bregman 2011; Dai et al. 2012; Anderson, Bregman & Dai 2013; Bogdán et al. 2013a,b; Anderson et al. 2014; Walker, Bagchi & Fabian 2014). The typical densities at galactocentric distances of ≥ 100 kpc is inferred to be a few times 10^{-4} cm^{-3} (e.g. Bogdán et al. 2013b), at a temperatures of $\sim$0.5 keV. The amount of material implied in this extended region is unlikely to come from the star formation process, as shown by Bogdán et al. (2013a). An extended region of circumgalactic medium (CGM) has also been observed through O VI absorption lines around massive galaxies at $z \leq 1$ (Tumlinson et al. 2011), although these observations probe clouds at $T \sim 10^{5.5}$ K.

At the same time, the presence of hot halo gas around the Milky Way Galaxy has been inferred via ram pressure arguments from the motion of satellite galaxies (Grcevich & Putman 2009; Putman,

★ E-mail: priyankas@rri.res.in

Peek & Joung 2012; Gatto et al. 2013). These observations suggest that the density profile of the hot coronal gas in our Galaxy is rather flat out to large radius, with $n \sim 10^{-3.5}$ cm^{-3}. Theoretically, one can understand this profile from simple modelling of hot, high-entropy gas in hydrostatic equilibrium (Maller & Bullock 2004; Sharma et al. 2012; Fang, Bullock & Boylan-Kolchin 2013). While in galaxy clusters, the high entropy of the diffuse gas produces a core, for massive galaxies (with implied potential wells shallower than in galaxy clusters), the core size is relatively large and extends to almost the virial radius.

One of the implications of this hot coronal gas in the haloes of massive galaxies is the Sunyaev–Zel'dovich (SZ) distortion of the cosmic microwave background radiation (CMBR; Planck Collaboration XI 2013). The average y-distortion of the CMBR from massive galaxies is likely to be small. However, the anisotropy power spectrum could have a substantial contribution from the hot gas in galactic haloes. The SZ distortion from galaxy clusters have been computed with the observed density and temperature profiles of the X-ray emitting gas, or the combined pressure profile (e.g. Majumdar 2001; Komatsu & Seljak 2002; Efstathiou & Migliaccio 2012). In the case of the galactic haloes, because of the expected flat density profile, the resulting y-distortion could be larger than that of galaxy clusters for angular scales that correspond to the virial radii of massive galaxies, i.e. $\ell \sim 10^4$. These angular scales are being probed now, and therefore the contribution to the SZ signal from galactic haloes is important. In this paper, we calculate the angular power spectrum from both the thermal Sunyaev–Zel'dovich (tSZ) and kinetic Sunyaev–Zel'dovich (kSZ) effects, if a fraction $f \sim 0.11$ of the total baryonic content of massive galaxies is in the form of hot or ionized halo gas.

Although such a fraction of gas has been estimated from the observations of NGC 1961 and NGC 6753 (Bogdán et al. 2013a), it remains uncertain whether it is a representative value, or whether it can be as low as 0.05. Recent studies of absorption from halo gas along the lines of sight to background quasars show that roughly half of the missing baryons is contained in the halo as warm (at $\sim 10^4$ and $\sim 10^{5.5}$ K) components. We also discuss the possible SZ signatures from this cool–warm gas in galactic haloes.

2 SZ DISTORTION FROM HOT GALACTIC HALO GAS

For simplicity, we assume that galactic haloes contain a constant fraction of the total halo mass, independently of the galaxy mass. If we consider the total baryon fraction $\Omega_b/\Omega_m \sim 0.16$, and the fraction of the total mass that is likely to be in the disc, which is predicted to be $\sim$0.05 (Mo, Mao & White 1998; Dutton et al. 2010; Leauthaud et al. 2010; Moster et al. 2010), then one can assume a fraction $f_{\rm gas} = 0.11$ of the total halo mass to be spread throughout the halo. We also assume it to be uniform in density, with a temperature given by the virial temperature of the halo. The uncertainties in gas fraction and temperature are explored later in Section 5.1. The cosmological parameters needed for our calculations are taken from the recent Planck results (table 2 of Planck Collaboration XVI 2014).

2.1 tSZ effect

When CMBR photons are inverse Compton scattered by high-energy electrons, the CMB spectrum is distorted giving rise to the tSZ effect. This effect is represented in terms of the Compton y-parameter defined as $y = (k_b T_e n_e \sigma_T L)/(m_e c^2)$ where σ_T is the Thomson scattering cross-section, T_e is the temperature ($T_e \gg T_\gamma$) and n_e is the electron density of the medium, considered to be uniform here, and ℓ is the distance traversed by the photons through the medium. The profile of y can be written in terms of the impact parameter w, or the angle $\theta = w/D_A$ (where D_A is the angular diameter distance) as

$$y(w) = \frac{2 k_b T_v n_e \sigma_T}{m_e c^2} \sqrt{R_v^2 - w^2}\,,$$
$$y(\theta) = \frac{2 k_b T_v n_e \sigma_T R_v}{m_e c^2} \sqrt{1 - \frac{D_A^2 \theta^2}{R_v^2}}. \quad (1)$$

Here, the electron density $n_e = \frac{\rho_{\rm gas}}{\mu_e m_p}$ of the hot gas is determined by the requirement that the total hot gas mass within the virial radius is a fraction $f_g = 0.11$ of the halo mass. The virial radius of a halo of mass M collapsing at redshift z is given by

$$R_{\rm vir} = 0.784 \left(\frac{M}{10^8\, h^{-1}}\right)^{1/3} \left(\frac{\Omega_M}{\Omega_M(z)} \frac{\triangle(z)}{8\pi^2}\right)^{-1/3} \times \left(\frac{1+z}{10}\right)^{-1} h^{-1}\,{\rm kpc}, \quad (2)$$

where $\Omega_M(z) = \Omega_M(1+z)^3/E^2(z)$, the critical overdensity $\triangle(z) = 18\pi^2 + 82d - 39d^2$ and $d = \Omega_M(z) - 1$.

Later, we will also discuss the effect of varying f_g, including its possible redshift evolution. The temperature T_e corresponds to the virial temperature of the halo. We discuss in Section 3.2 below the appropriate mass and redshift range of galactic haloes in which the gas likely remains hot.

2.2 kSZ effect

If the scattering medium has bulk velocity with respect to the CMB frame, the CMBR is anisotropic in the rest frame of the scattering medium. The scattering makes the CMBR isotropic in the rest frame of the scattering medium, resulting in the distortion of the CMB spectrum with respect to the observer and giving rise to the kSZ effect. The kSZ effect is proportional to the line-of-sight peculiar velocity and optical depth of the scattering medium. In the non-relativistic limit, the Compton y-parameter for the kSZ effect is defined as $y = (v_{\rm los} n_e \sigma_T L)/c$, where $v_{\rm los}$ is the line-of-sight peculiar velocity of the scattering medium. The tSZ effect and the kSZ effect have different frequency dependences which makes them easily separable with good multifrequency data. In contrast to the tSZ effect, the spectral shape of the CMB is unchanged by the kSZ effect. In the Rayleigh–Jeans limit, the ratio of the change in CMB temperature caused by these two effects is

$$\frac{\Delta T_{\rm kin}}{\Delta T_{\rm th}} \approx \frac{1}{2}\frac{v_{\rm los}}{c}\left(\frac{k_b T_e}{m_e c^2}\right)^{-1}, \approx 0.09 \left(\frac{v_{\rm los}}{1000\,{\rm km\,s^{-1}}}\right)\left(\frac{k_b T_e}{10\,{\rm keV}}\right)^{-1}. \quad (3)$$

For galaxy clusters, $k_b T_e \sim 10$ keV and $v_{\rm los} \sim$ a few hundred km s^{-1} which makes tSZ $\gg$ kSZ. But for the case of galaxies with virial temperature $T_e \sim 10^6$ K, hence $k_b T_e \sim 0.1$ keV, thus making kSZ > tSZ.

3 THE SZ POWER SPECTRUM

The SZ power spectrum arises by summing over the contributions from *all* the haloes that would distort the CMB convolved with the template distortion for the haloes as a function of mass and

redshift; the distribution of the haloes can be approximated by fits to outputs from *N*-body simulations. However, not all dark matter haloes identified in the simulations would contribute to the SZ C_ℓ, and one has to use *only* those galactic haloes where the gas has not cooled substantially; this is discussed in detail in Section 3.2.

3.1 tSZ C_ℓ

The tSZ template for contribution by a galactic halo is given by the angular Fourier transform of $y(\theta)$ (see equation 1) and is given by

$$\begin{aligned} y_l &\approx 2\pi \int_0^\pi \theta\, y(\theta) J_o[(l+1/2)\theta]\mathrm{d}\theta\,, \\ &= \frac{4\pi k_b \sigma_\mathrm{T} R_v}{m_\mathrm{e} c^2} \int_0^\pi \theta\, T_v n_\mathrm{e} \sqrt{1-\frac{D_\mathrm{A}^2\theta^2}{R_v^2}}\, J_o[(l+1/2)\theta]\mathrm{d}\theta \\ &= \frac{8 k_b T_v n_\mathrm{e} \sigma_\mathrm{T} R_v^{3/2}}{m_\mathrm{e} c^2 D_\mathrm{A}^{1/2}} \left(\frac{\pi}{2l+1}\right)^{3/2} J_{3/2}\left[(l+1/2)\frac{R_v}{D_\mathrm{A}}\right]. \end{aligned} \tag{4}$$

The last equality follows from Gradshteyn & Ryzhik (1990).

The angular power spectrum due to the tSZ effect by hot diffuse gas in galactic haloes is given by

$$C_\ell = g^2(x) C_\ell^{yy}, \tag{5}$$

where $g(x) = x\coth(x/2) - 4$ and C_ℓ^{yy} is frequency independent power spectrum.

$$C_\ell^{yy} = C_\ell^{yy(\mathrm{P})} + C_\ell^{yy(\mathrm{C})}, \tag{6}$$

where $C_\ell^{yy(\mathrm{P})}$ is the Poisson term and $C_\ell^{yy(\mathrm{C})}$ is clustering or correlation term. These two terms can be written as (Komatsu & Kitayama 1999)

$$\begin{aligned} C_\ell^{yy(\mathrm{P})} &= \int_0^{z_\mathrm{max}} \mathrm{d}z \frac{\mathrm{d}V}{\mathrm{d}z} \int_{M_\mathrm{min}}^{M_\mathrm{max}} \mathrm{d}M \frac{\mathrm{d}n(M,z)}{\mathrm{d}M} |y_l(M,z)|^2 \\ C_\ell^{yy(\mathrm{C})} &= \int_0^{z_\mathrm{max}} \mathrm{d}z \frac{\mathrm{d}V}{\mathrm{d}z} P_\mathrm{m}(k=\frac{l}{r(z)},z) \\ &\quad \times \left[\int_{M_\mathrm{min}}^{M_\mathrm{max}} \mathrm{d}M \frac{\mathrm{d}n(M,z)}{\mathrm{d}M} b(M,z) y_l(M,z)\right]^2. \end{aligned} \tag{7}$$

Here, $r(z) = (1+z)D_\mathrm{A}$ is the comoving distance, $\frac{\mathrm{d}V}{\mathrm{d}z}$ is differential comoving volume per steradian, $P_\mathrm{m}(k, z)$ is matter power spectrum, $b(M, z)$ is the linear bias factor, and $\frac{\mathrm{d}n(M,z)}{\mathrm{d}M}$ is the differential mass function. Here, we have used the Sheth–Tormen (ST) mass function

$$\begin{aligned} \frac{\mathrm{d}n}{\mathrm{d}M}\mathrm{d}M &= A\sqrt{\frac{2\alpha\nu^2}{\pi}} \frac{\rho_m}{M^2} \mathrm{e}^{-\alpha\nu^2} \left[-\frac{\mathrm{d}\log\sigma}{\mathrm{d}\log M}\right] \\ &\quad \times \left[1+\left(\alpha\nu^2\right)^{-p}\right] \mathrm{d}M\,, \end{aligned} \tag{8}$$

where $A = 0.322\,184$, $\alpha = 0.707$ and $p = 0.3$ (Sheth, Mo & Tormen 2001). We have used the bias factor from Jing (1999),

$$b(M,z) = \left(1+\frac{0.5}{\nu^4}\right)^{(0.06-0.02n)} \left(1+\frac{\nu^2-1}{\delta_\mathrm{c}}\right), \tag{9}$$

with $\nu = \frac{\delta_c}{D_\mathrm{g}(z)\sigma(M)}$, where $D_\mathrm{g}(z)$ is the growth factor, n is the index of primordial power spectrum, $\delta_\mathrm{c} = 1.68$ is the critical overdensity and $\sigma(M)$ is the present-day smoothed (with top hat filter) variance.

3.2 Mass and redshift range

As mentioned earlier, not all the galactic haloes given by the ST mass function (i.e. equation 8) will contribute to the SZ C_ℓ. For a realistic estimate of the CMB distortion from circumgalactic gas in galaxies, we need to use only those galactic haloes in which the hot halo gas does not cool substantially, so that the hot gas persists for a considerable period of time and can contribute to the anisotropy. The cooling time of the gas is defined as $t_\mathrm{cool} = 1.5nkT/(n_\mathrm{e}^2\Lambda(T))$, where n is the particle density ($\sim\frac{\mu_\mathrm{e}}{\mu} n_\mathrm{e}$), μ is mean molecular weight of the gas, μ_e is the mean molecular weight per free electron and $\Lambda(T)$ is the cooling function. We assume the galactic halo gas to be of metallicity 0.1 $\mathrm{Z}_\odot$, and use the cooling function from Sutherland & Dopita (1993).

This cooling time should be compared with a time-scale corresponding to the destruction of these galactic haloes in the merger or accretion processes, which would lead to the formation of larger haloes. Every merging event leads to heating of the halo gas back to the virial temperature. It is therefore reasonable to assume that the halo gas would remain hot at the virial temperature if the cooling time is longer than the time corresponding to the destruction of haloes.

We have used an excursion set approach to calculate the destruction time (Lacey & Cole 1993, 1994). For a Press–Schechter mass function, the destruction time for a galactic halo of mass M at time t is

$$\begin{aligned} t_\mathrm{dest}(M,t) &= [\phi(M,t)]^{-1}\,, \\ &= \left[\int_{M(1+\epsilon)}^\infty \tilde{Q}(M, M_1; t)\mathrm{d}M_1\right]^{-1}, \end{aligned} \tag{10}$$

where $\tilde{Q}(M, M_1; t)$ is the probability that an object of mass M grows into an object of mass M_1 per unit time through merger or accretion at time t

$$\begin{aligned} \tilde{Q}(M, M_1; t)\mathrm{d}M_1 &= \sqrt{\frac{2\sigma^2(M_1)}{\pi}} \left[\frac{\sigma^2(M)}{\sigma^2(M_1)(\sigma^2(M)-\sigma^2(M_1))}\right]^{3/2} \\ &\quad \times \left|\frac{\mathrm{d}\delta}{\mathrm{d}t}\right| \exp\left[-\frac{\delta^2(\sigma^2(M)-\sigma^2(M_1))}{2\sigma^2(M)\sigma^2(M_1)}\right] \\ &\quad \times \left|\frac{\mathrm{d}\sigma(M_1)}{\mathrm{d}M_1}\right| \mathrm{d}M_1. \end{aligned} \tag{11}$$

Here, we have used $\epsilon = 0.1$. For the mass range considered, the destruction time for ST mass function and Press–Schechter mass function give similar results (Mitra et al. 2011). For simplicity, we have used the Press–Schechter mass function to calculate the destruction time.

We show the ratio of the cooling time to destruction time-scale as a function of mass at different redshifts in Fig. 1. Based on this estimate, we use those galactic haloes in our calculation of CMBR anisotropy for which $t_\mathrm{cool}/t_\mathrm{dest} \geq 1$, so that gas in these galactic haloes cannot cool quickly. This condition is used to determine the lower mass limit of galactic haloes M_min in equation (7). We have used $M_\mathrm{max} = 10^{13}\,h^{-1}\,\mathrm{M}_\odot$ for the upper mass limit. For upper redshift limit of integration in equation (7), it is sufficient to take $z_\mathrm{max} = 8$ (see Fig. 4).

3.3 kSZ C_ℓ

Analogously to the tSZ effect, the angular Fourier transform of Compton y-parameter for the kSZ effect is given by

$$y_l \approx 8\frac{v_\mathrm{los}}{c} \frac{n_\mathrm{e}\sigma_\mathrm{T} R_v^{3/2}}{D_\mathrm{A}^{1/2}} \left(\frac{\pi}{2l+1}\right)^{3/2} J_{3/2}\left[(l+1/2)\frac{R_v}{D_\mathrm{A}}\right]. \tag{12}$$

A crucial input into the calculation of the kSZ C_ℓ is the line-of-sight peculiar velocity the dark matter halo which depends on

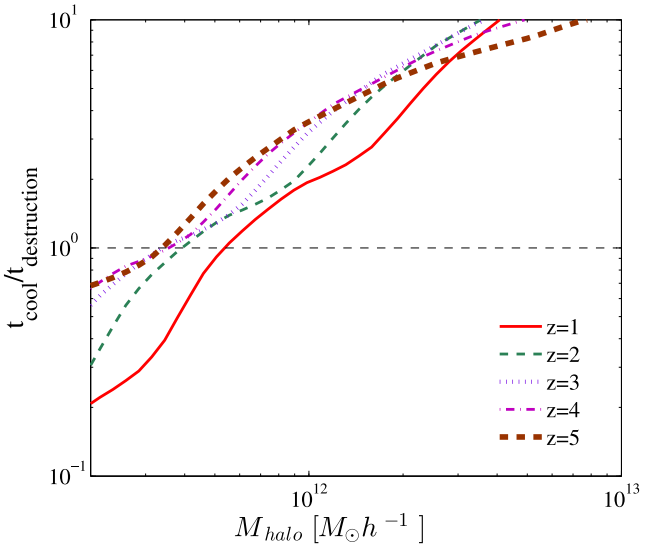

Figure 1. The ratio of cooling time to destruction time-scale of haloes is shown as a function of halo mass collapsing at $z = 1$ (red solid line), $z = 2$ (thin green dashed line), $z = 3$ (blue dotted line), $z = 4$ (magenta dot–dashed line) and $z = 5$ (thick brown dashed line).

its mass M, redshift and the overdensity of the environment δ in which the halo is present (Sheth & Diaferio 2001; Hamana et al. 2003; Bhattacharya & Kosowsky 2008). The probability distribution function of the line-of-sight velocity of a halo with mass M located in a region of overdensity δ is

$$p(v_{\rm los}|M,\delta,a) = \sqrt{\frac{3}{2\pi}}\frac{1}{\sigma_v(M,a)}\exp\left(-\frac{3}{2}\left[\frac{v}{\sigma_v(M,a)}\right]^2\right) \quad (13)$$

with the 3D velocity dispersion given by

$$\begin{aligned}\sigma_v(M,a) &= [1+\delta(R_{\rm local})]^{\mu(R_{\rm local})}\sigma_{\rm p}(M,a)\,,\\ &= [1+\delta(R_{\rm local})]^{\mu(R_{\rm local})}aH(a)D_a\left(\frac{{\rm d}\ln D_a}{{\rm d}\ln a}\right)\\ &\quad\times\left(1-\frac{\sigma_0^4(M)}{\sigma_{-1}^2(M)\sigma_1^2(M)}\right)^{1/2}\sigma_{-1}(M)\,, \end{aligned} \quad (14)$$

where $\sigma_{\rm p}(M, a)$ is the rms peculiar velocity at the peaks of the smoothed density field and σ_js are the moments of initial mass distribution defined as

$$\sigma_j^2(M) = \frac{1}{2\pi^2}\int_0^\infty {\rm d}k k^{(2+2j)}P(k)W^2(kR(M))\,. \quad (15)$$

Here, the smoothing scale $R(M)$ is given by $\left(\frac{3M}{4\pi\rho_{\rm m}}\right)^{1/3}$, $W(kR)$ is the top hat filter and $\rho_{\rm m}$ is the present-day mean matter density. The dependence of peculiar velocity on its environment is contained in parameters $R_{\rm local}$, $\mu(R_{\rm local})$ and $\delta(R_{\rm local})$. These parameters are obtained by the conditions (Bhattacharya & Kosowsky 2008)

$$\mu(R_{\rm local}) = 0.6\frac{\sigma_0^2(R_{\rm local})}{\sigma_0^2(10\,{\rm Mpc}\,h^{-1})}\,, \quad (16)$$

with $\sigma_0(R_{\rm local}) = 0.5/\sqrt{(1+z)}$ and $\delta(R_{\rm local}) = \sqrt{\sigma_0(R_{\rm local})}$.

The angular power spectrum due to kSZ effect by this hot diffuse gas is independent of frequency and is given by

$$C_l^{yy} = C_l^{yy({\rm P})} + C_l^{yy({\rm C})}, \quad (17)$$

where $C_l^{yy({\rm P})}$ and $C_l^{yy({\rm C})}$ are Poisson and clustering terms given by equation (7).

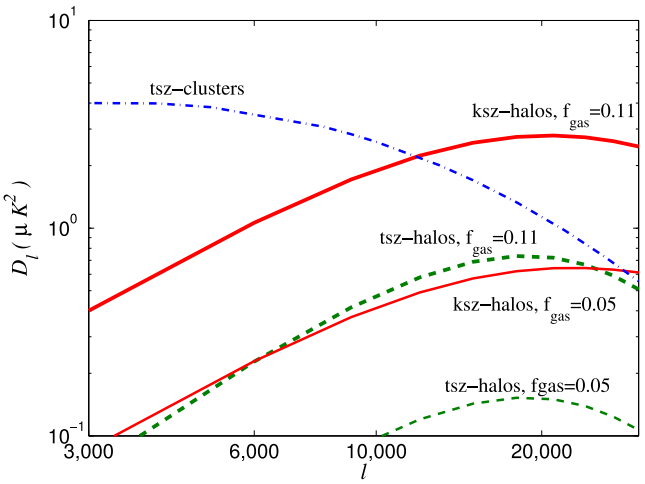

Figure 2. Angular power spectrum of CMBR at 150 GHz over a larger range of ℓ, for tSZ (green dashed line) and kSZ (red solid line) from galactic haloes, compared with tSZ from clusters (blue dot–dashed line). Here, the thick and thin lines correspond to $f_{\rm gas} = 0.11$ and $f_{\rm gas} = 0.05$, respectively.

3.4 SZ from CGM versus SZ from ICM

We plot the multipole dependence of both tSZ and kSZ C_ℓ from the CGM, in Fig. 2, in term of the parameter $D_l = \frac{l(l+1)}{2\pi}C_\ell\overline{T}^2_{\rm CMB}$, where $\overline{T}_{\rm CMB}$ is present day mean CMB temperature in the units of μK. In the same figure, we also plot the tSZ C_ℓ from hot gas in clusters of galaxies, the kinetic SZ C_ℓ from intracluster medium (ICM) being subdominant. We find that SZ C_ℓ's from CGM peak above $\ell \sim 15\,000$, whereas the tSZ from ICM peaks at $\ell \sim 3000$ and then falls at higher ℓ-values. The tSZ signal from CGM dominates that from ICM over $\ell > 30\,000$, whereas the kSZ from galactic haloes overtakes tSZ from clusters earlier at $\ell > 10\,000$.

We have overplotted South Pole Telescope (SPT) and Atacama Cosmology Telescope (ACT) data, with grey and black bars, respectively, and autocorrelation lines from fig. 4 of Addison, Dunkley & Spergel (2012) on top of SZ C_ℓ from galactic haloes for a smaller range $3000 < \ell < 10\,000$ in Fig. 3. The figure shows the contribution from tSZ and kSZ from galactic haloes with red solid (thick) and blue solid (thick) lines. For comparison, the tSZ and kSZ signals from galaxy clusters are shown as red and blue solid (thin) lines. Also, the contribution from the sources responsible for the cosmic infrared background (CIB) are shown, for both Poisson (brown dashed line) and the clustered case (brown dot–dashed line). The contribution from clustering of radio sources is shown in green as a dotted line. The lensed primary signal is shown as a black dashed line. The comparison of tSZ and kSZ signals from galactic haloes and galaxy clusters show that kSZ signal from galactic haloes become comparable to galaxy cluster signals at $\ell \sim 10\,000$. This is because of the fact that kSZ is more important for lower mass haloes, which correspond to smaller angles and larger ℓ-values.

3.5 Redshift distribution of the angular power spectrum

The redshift distribution of C_ℓ can be determined using

$$\frac{{\rm d}\ln C_\ell}{{\rm d}\ln z} = \frac{z\frac{{\rm d}V}{{\rm d}z}\int{\rm d}M\frac{{\rm d}n(M,z)}{{\rm d}M}|y_l(M,z)|^2}{\int{\rm d}z\frac{{\rm d}V}{{\rm d}z}\int{\rm d}M\frac{{\rm d}n(M,z)}{{\rm d}M}|y_l(M,z)|^2}. \quad (18)$$

We show the redshift distribution of C_ℓ for $\ell = 3000$, 6000, 10 000 and 20 000 for tSZ and kSZ effect in Fig. 4. For tSZ effect (shown in thin lines), for $\ell = 3000$, C_ℓ has a peak at $z \sim 2$. This peak shifts

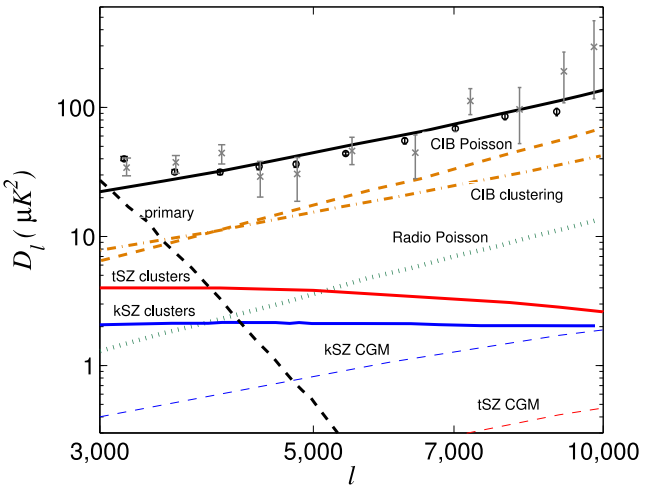

Figure 3. Angular power spectrum of CMBR at 150 GHz from different processes and compared with data points from ACT (grey bars) and SPT (black bars). The tSZ from galactic haloes calculated here is shown in red (thick solid line), and the kSZ from galactic haloes is shown in blue (thick solid line). tSZ from galaxy clusters (Efstathiou & Migliaccio 2012) is shown in red (thin solid line), the kSZ from galaxy clusters is shown in blue (thin solid line), the radio Poisson and CIB Poisson signals in green dotted and brown dashed lines, respectively, and CIB clustering signal is shown by a brown dot–dashed line. The lensed primary signal is shown in black, and the total signal is shown by a grey line.

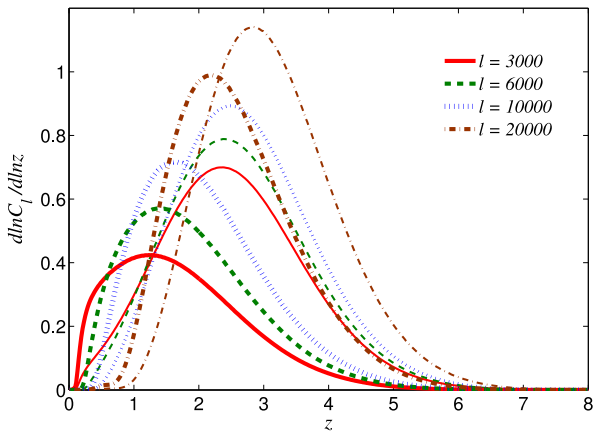

Figure 4. Redshift distribution of tSZ and kSZ effects. tSZ cases are shown with thin lines and kSZ cases, with thick lines for $l = 3000$ (red solid lines), $l = 6000$ (green dashed lines), $l = 10\,000$ (blue dotted lines) and $l = 20\,000$ (brown dot–dashed lines).

to higher redshifts with increasing value of ℓ. For all ℓ-values ($\ell >$ 3000) there is non-negligible contribution to C_ℓ coming from $z >$ 5.

In case of the kSZ effect (thick lines), for $\ell = 3000$ there is a broad peak around $z \sim$ 1–2 and, the contribution to C_ℓ is significant even below $z = 1$. The peak shifts to higher redshifts with increasing value of ℓ. The contribution from higher redshift becomes more important for larger ℓ-values. Note that C_ℓ scales as the square of the fraction of hot gas in galactic haloes, and the plotted values assume the fraction to be 0.11. If the fraction is smaller, the values of C_ℓ for kSZ and tSZ are correspondingly lower. For example, if the hot halo gas constitutes only half of the missing baryons, with a fraction ∼0.05 (instead of 0.1), then SZ signal from galactic haloes would dominate at $\ell \geq 30\,000$ (instead of 10^4).

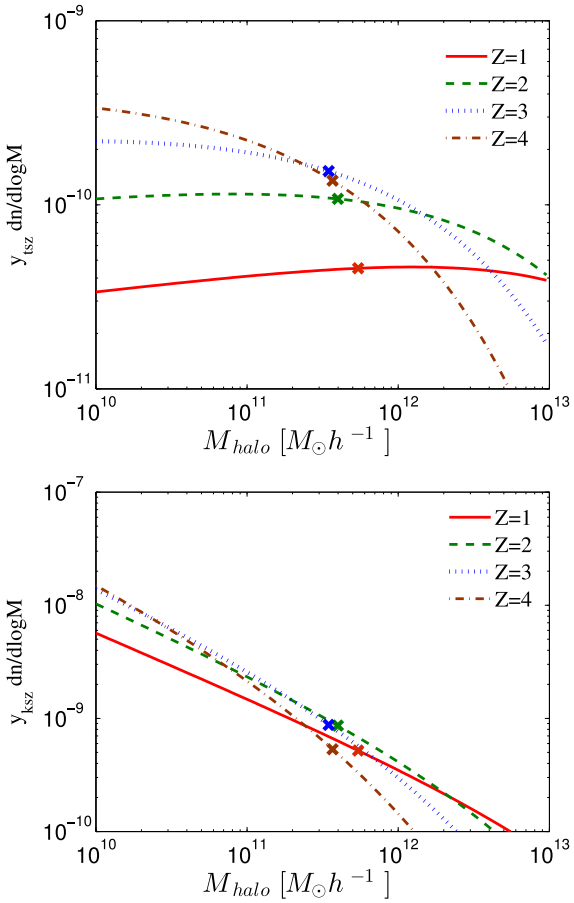

Figure 5. Moments of the mass function for tSZ (top panel) and kSZ (bottom panel), as a function of galactic halo masses, for redshifts $z = 1$ (red solid line), $z = 2$ (green dashed line), $z = 3$ (blue dotted line) and $z = 4$ (brown dot–dashed line). The cross markers on each line show that the lower limits of masses considered in the calculations of SZ signal based on the cooling time-scale being longer than halo destruction time-scale.

3.6 Mass distribution

We can estimate the range of masses which contribute most to the tSZ and kSZ effects, by computing appropriate moments of the mass function, for pressure and peculiar velocity. Fig. 5 shows the moment of y-parameters for tSZ and kSZ in the top and bottom panels, respectively, for the mass range 10^{10}–$10^{13}\ h^{-1}\ \mathrm{M}_\odot$, corresponding to the l-range $\sim 7 \times 10^4$–7×10^3 for $z = 1$, and l-range $\sim 1.4 \times 10^5$–1.4×10^4 for $z = 4$. The moments of tSZ ($y_{\mathrm{tSZ}} \times \frac{\mathrm{d}N}{\mathrm{d}\log M}$) show that the dominant mass range decreases with increasing redshift, from being $\sim 10^{13}\ h^{-1}\ \mathrm{M}_\odot$ at $z \sim 1$, to haloes of $\sim 5 \times 10^{11}\ h^{-1}\ \mathrm{M}_\odot$ at $z \sim$ 2–3 to lower masses at higher redshift. From the redshift distribution information in Fig. 4, we can infer that galactic haloes with mass $\sim 10^{12}\ h^{-1}\ \mathrm{M}_\odot$ are the dominant contributors for $\ell \leq 10^4$ for tSZ effect.

The moments of the kSZ signal ($y_{\mathrm{kSZ}} \times \frac{\mathrm{d}N}{\mathrm{d}\log M}$) show that low-mass galactic haloes are the major contributors to the signal, and become progressively more important at increasing redshifts. Since we have constrained the mass range from a cooling time-scale argument, the moments at different redshift show that the dominant mass is $\sim 5 \times 10^{11}\ h^{-1}\ \mathrm{M}_\odot$ for $z \sim$ 1–3. Again, from the redshift distribution information in Fig. 4, this implies that galactic haloes with $\sim 10^{12}\ h^{-1}\ \mathrm{M}_\odot$ are the major contributors, as in the case of tSZ effect. Since significant contribution for tSZ and kSZ comes

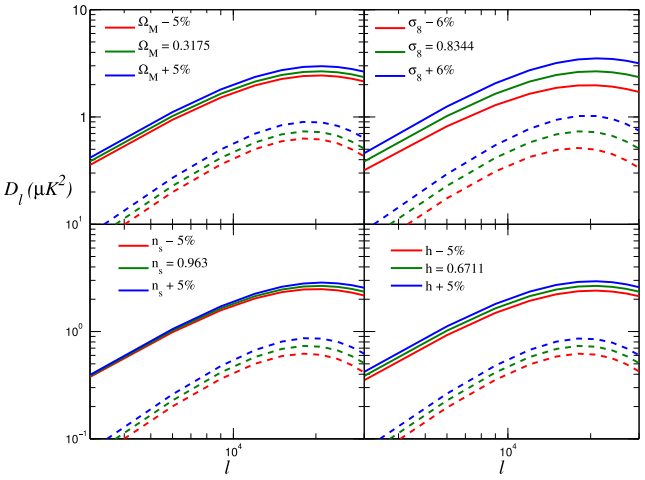

Figure 6. Dependence of SZ angular power spectrum on σ_8, Ω_M, n_s and h. Here, the dashed lines are tSZ effect and the solid lines represent kSZ effect.

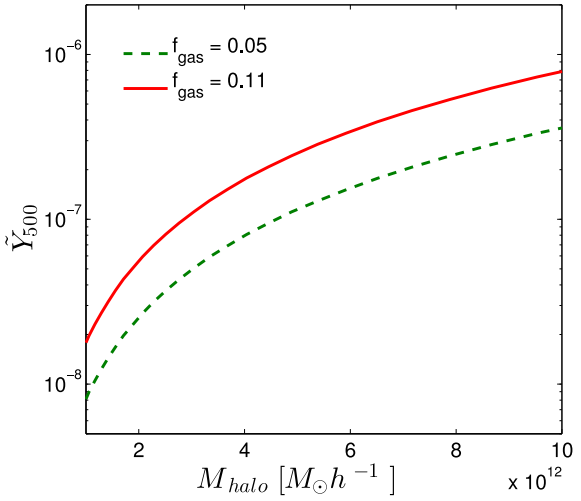

Figure 7. $\tilde{Y}_{500}$ as a function of halo mass (red solid line) for $f_{gas} = 0.11$ and $f_{gas} = 0.05$ (green dashed line).

from low-mass haloes, our predictions are sensitive to the assumed lower mass in which the hot halo gas can remain hot until the next merging event.

3.7 Dependence of SZ angular power spectrum on cosmological parameters

We also calculate the dependence of the SZ angular power spectrum on different cosmological parameters. In Fig. 6, we plot the dependences of tSZ and kSZ signals on σ_8, Ω_M, n_s and h with dashed and solid lines, respectively. When one cosmological parameter is varied, others are kept fixed. However, when Ω_M is varied, Ω_Λ is also changed to keep $\Omega_M + \Omega_\Lambda = 1$.

The dependences of C_ℓ on different cosmological parameters can be fitted by power-law relations near the fiducial values of the corresponding parameters. For example, we find that near the fiducial value of σ_8, $C_\ell \propto {\sigma_8}^6$, which is similar to the dependence of tSZ signal from galaxy clusters (Komatsu & Seljak 2002). For other parameters, we have, for tSZ, $C_\ell \propto {\Omega_M}^3$, $C_\ell \propto {n_s}^{7/2}$ and $C_\ell \propto h^3$ for tSZ. The corresponding dependences for kSZ are $C_\ell \propto {\sigma_8}^5$, $C_\ell \propto {\Omega_M}^2$, $C_\ell \propto n_s$ and $C_\ell \propto h^2$.

4 DETECTABILITY IN FUTURE SURVEYS AND CONSTRAINING GAS PHYSICS

4.1 Integrated Comptonization parameter $\tilde{Y}_{500}$

Next, we estimate the integrated Comptonization parameter for CGM. The Comptonization parameter Y_{500} (due to tSZ) integrated over a sphere of radius R_{500} is

$$Y_{500} = \frac{\sigma_T}{m_e c^2} \int_0^{R_{500}} \frac{P\,dV}{D_A^2(z)} = \frac{\sigma_T n_e k_b T_e}{m_e c^2 D_A^2(z)} \frac{4\pi R_{500}^3}{3}, \quad (19)$$

where $D_A^2(z)$ is the angular diameter distance, $P = n_e k_b T_e$ is pressure of electron gas and R_{500} is defined as the radius within which the mean mass density is 500 times the critical density of the Universe. The second equality in the above equation is for the case of constant electron density and temperature. The integrated Comptonization parameter scaled to $z = 0$ is defined as

$$\tilde{Y}_{500} \equiv Y_{500} E^{-2/3}(z) \left(\frac{D_A(z)}{500\,\mathrm{Mpc}} \right)^2. \quad (20)$$

Here, $\tilde{Y}_{500}$ and Y_{500} are expressed in square arcmin. We show in Fig. 7 the values of $\tilde{Y}_{500}$ as a function of halo mass for gas fractions $f_{0.11}$ and $f_{gas} = 0.05$. We have used the fit for concentration parameter (c) as a function of halo mass from Duffy et al. (2008).

From table 1 of Planck Collaboration XI (2013), the lowest stellar mass bin for which SZ signal has been detected ($\tilde{Y}_{500} \sim 10^{-6}$ arcmin^2) is $M_* \sim 4 \times 10^{12}\,M_\odot$. This stellar mass corresponds to a virial mass $\sim 4.25 \times 10^{12}\,M_\odot\,h^{-1}$. From our calculations for a galactic halo of $M_{vir} \sim 4.25 \times 10^{12}\,M_\odot\,h^{-1}$ with $f_{gas} = 0.11$, the $\tilde{Y}_{500} \sim 0.2$–0.3×10^{-6} arcmin^2, consistent with the observed values (table 1 of Planck Collaboration XI 2013). If we use $f_{gas} = 0.05$, $\tilde{Y}_{500}$ goes down by roughly a factor of 2.

4.2 SNR in future surveys

The detectability of the CMB distortion from circumgalactic baryons can be estimated by calculating the cumulative signal-to-noise ratio (SNR) of the SZ power spectrum for a particular survey. For our purpose, we focus on two types of surveys, one which is an extension of the ongoing SPT survey to higher multipoles (although we show that the SNR from $\ell > 15\,000$ does not add much to the cumulative SNR), and a more futuristic survey which covers 1000 deg^2 of the sky (i.e. $f_{sky} \sim 2$ per cent) and is cosmic variance error limited. These are labelled 'SPT-like' and 'CV1000', respectively, for the rest of the paper.

(1) SPT-like survey: In this case, we use $\ell_{min} = 3000$ and $\ell_{max} = 30\,000$. The noise in the measurement of C_ℓs (i.e. $\triangle C_\ell$) is taken from actual SPT data (fig. 4 of Addison et al. 2012). These errors are then fitted with a power-law dependence on ℓ and extrapolated till $\ell = 30\,000$.

(2) CV1000 survey: This survey has 2 per cent sky coverage, and the error on C_ℓs are cosmic variance limited. Here, we have used a smaller ℓ-range and have taken $\ell_{min} = 6000$ and $\ell_{max} = 9000$.

The cumulative SNR, for SZ C_ℓ between ℓ_{min} and ℓ_{max}, is given by

$$\mathrm{SNR}_{cumu}(\ell_{min} < \ell_{max}) = \left(\Sigma_{\ell_{min}\ell'_{min}}^{\ell_{max}} C_\ell^X (M_{\ell\ell'}^X)^{-1} C_{\ell'}^X \right)^{1/2}, \quad (21)$$

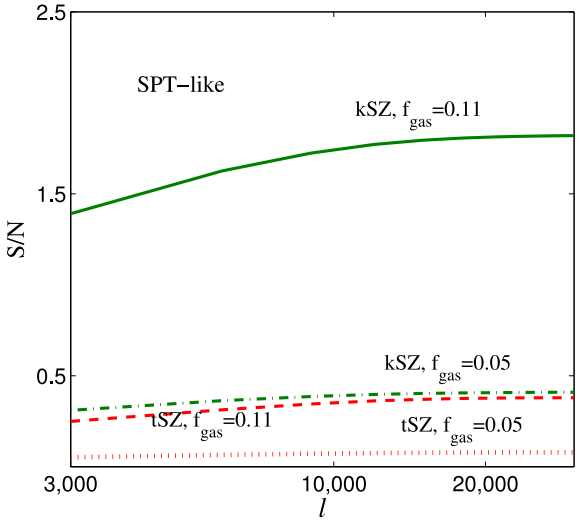

Figure 8. The cumulative SNR as a function of $\ell_{\rm max}$, in case of SPT-like survey, with $\ell_{\rm min} = 3000$. The upper line corresponds to kSZ and the lower line to tSZ. The solid (green) and dashed (red) lines corresponds to kSZ and tSZ for $f_{\rm gas} = 0.11$, respectively, and the dot–dashed (green) and dotted (red) lines, for $f_{\rm gas} = 0.05$.

where X denotes cases tSZ, kSZ or Total, i.e. tSZ+kSZ, and $M^{\rm X}_{\ell\ell'}$ is the corresponding covariance matrix, for any particular survey, given by

$$M^X_{\ell\ell'} = \frac{1}{4\pi f_{\rm sky}} \left(\frac{4\pi (C^X_\ell + N_\ell)^2}{(\ell + 1/2)\triangle\ell} \delta_{\ell\ell'} + T^X_{\ell\ell'} \right), \quad (22)$$

where N_ℓ is the noise power spectrum (after foreground removal) and $T^X_{\ell\ell'}$ is the SZ angular trispectrum (see, e.g. Komatsu & Kitayama 1999). Note that this formula for the covariance matrix neglects the 'halo sample variance'.

The cumulative SNR provides a simple way to assess the constraining power of a given experiment irrespective of the constraints on particular parameters. We compute the cumulative SNR's for our two surveys, SPT-like and CV1000 surveys. Fig. 8 shows the SNR as a function of $\ell_{\rm max}$ for the SPT-like survey. Note that the covariance matrix in equation (21), in principle, should include all contributions from cosmic variance (Gaussian and non-Gaussian), experimental noise after foreground removal, as well as the trispectrum which represents the sample variance contribution to the covariance. However, for the halo masses of interest and the ℓ range of the contribution of the SZ discussed in this paper, the trispectrum can be neglected and the covariance matrices are, effectively, diagonal. For the CV1000 survey, the diagonal covariance matrix only contains the cosmic variance errors. The covariance matrix, for the SPT-like survey, is taken to be the noise (actual error bar) reported by the SPT and extrapolated to higher ℓs (as explained earlier). In general, our extrapolation of SPT errors to higher ℓ-values are conservative in nature as seen in Fig. 8 – due to the increasing observational errors for higher multipoles, the SNR for the SPT-like survey flattens off beyond $\ell_{\rm max} \sim 15\,000$. It is also evident from the figure, that although it would need a stringent handle on astrophysical systematics and better modelling of SZ C_ℓ from galaxy clusters to separate out the tSZ C_ℓ from CGM, kSZ signal from CGM has an SNR $\sim 2\sigma$ for the SPT-like survey. If we take $l_{\rm min} = 10\,000$ for SPT-like survey, the SNR goes down roughly by a factor of 2. In comparison, for the more futuristic CV1000 survey, the tSZ and the kSZ signal can be detected with an SNR of ∼600(950), at (up to) $\ell_{\rm max} \sim 6000(9000)$.

Table 1. Fiducial values and priors on the parameters.

Parameter	Fiducial value	Prior-1	Prior-2	Prior-3
σ_8	0.8344	0.027	0.027	0.027
$\Omega_{\rm M}$	0.3175	0.020	0.020	0.020
$n_{\rm s}$	0.963	0.0094	0.0094	0.0094
h	0.6711	0.014	0.014	0.014
$f_{\rm tratio}$	1.0	–	1.0	1.0
$f_{\rm Temp}$	1.0	–	–	0.25
$f_{\rm gas}$	0.11	–	–	–
$\alpha_{\rm gas}$	0.0	–	–	–

5 FORECASTING

5.1 Formalism

We now employ the Fisher matrix formalism to forecast the expected constraints on the following parameters, focusing especially on the parameters related to gas physics of the circumgalactic baryons. The Fisher parameters considered are

$$\{[\sigma_8, \Omega_{\rm M}, n_{\rm s}, h], [f_{\rm gas}, f_{\rm tratio}, f_{\rm Temp}, \alpha_{\rm gas}]\}, \quad (23)$$

where the first set within the parenthesis is the cosmological parameters and the second set, which depends on baryonic physics, is the *astrophysical* parameters.

To construct the Fisher matrices for the two surveys, we compute the derivatives of the tSZ, kSZ and, hence, total SZ C_ℓ with respect to each parameter around the fiducial values listed in Table 1. Here, $f_{\rm gas}$ is the redshift-independent fraction of halo mass in gaseous form and $\alpha_{\rm gas}$ captures any possible evolution of the gas defined through $f_{\rm gas}(z) = f_{\rm gas}[E(z)]^{\alpha_{\rm gas}}$. Our fiducial model assumes no evolution of the gas fraction, see details in Section 5.2.1. The other two parameters that encapsulate the uncertainty in our knowledge of hot gas in galactic haloes are $f_{\rm tratio} = \frac{t_{\rm cool}}{t_{\rm dest}}$, i.e. the ratio of cooling time to destruction time for galactic haloes, $f_{\rm Temp} = \frac{T}{T_{\rm vir}}$, i.e. the ratio of the temperature of the gas to the virial temperature of gas in a halo.

For a given fiducial model, the Fisher matrix is written as

$$F_{ij} = \frac{\partial C^X_\ell}{\partial p_i} (M^X_{\ell\ell'})^{-1} \frac{\partial C^X_{\ell'}}{\partial p_j}, \quad (24)$$

where $M_{ll'}$ is given by equation 22 in case of CV1000 survey, and for SPT-like survey we have $M_{ll} = (\Delta C^{\rm SPT}_\ell)^2$. Here, $\Delta C^{\rm SPT}_\ell$s are the error on C_ℓs from SPT data. The fiducial values and the priors used are listed in Table 1. Note that in all our calculations, cosmological priors are always applied. Priors related to gas/halo physics are additionally applied, on a case by case basis. For the rest of the paper, we denote the different priors uses as follows.

Prior-1: Priors on cosmological parameters only.
Prior-2: Priors on cosmological parameters + 100 per cent prior on $f_{\rm tratio}$.
Prior-3: Priors on cosmological parameters + 100 per cent prior on $f_{\rm tratio}$ + 25 per cent prior on $f_{\rm Temp}$.

In Prior-3 and Prior-2, we have assumed a 100 per cent prior on $f_{\rm tratio}$, reflecting the maximum uncertainty in this parameter. For $f_{\rm Temp}$, we have assumed a smaller uncertainty, since our constraint that cooling time is longer than the destruction time ensures that the gas temperature to be close to the virial temperature.

Table 2. Error on parameters for different surveys and Prior cases with fixed $\alpha_{\rm gas}$.

Parameters	CV1000, P1	CV1000, P2	CV1000, P3	SPT-like, P1	SPT-like, P2	SPT-like, P3
$\Delta\sigma_8$	0.0166	0.0163	0.0162	0.0270	0.0270	0.0270
$\Delta\Omega_{\rm M}$	0.0163	0.0161	0.0161	0.020	0.020	0.020
$\Delta n_{\rm s}$	0.0093	0.0093	0.0093	0.0094	0.0094	0.0094
Δh	0.0139	0.0139	0.0139	0.0140	0.0140	0.0140
$\Delta f_{\rm tratio}$	0.2329	0.2268	0.2266	18.7380	0.9986	0.9982
$\Delta f_{\rm Temp}$	0.0312	0.0311	0.0309	1.6547	1.4826	0.2465
$\Delta f_{\rm gas}$	0.0023	0.0023	0.0023	0.1119	0.0433	0.0366

Table 3. Error on parameters for different surveys and Prior cases.

Parameters	CV1000, P1	CV1000, P2	CV1000, P3	SPT-like, P1	SPT-like, P2	SPT-like, P3
$\Delta\sigma_8$	0.0270	0.0263	0.0261	0.0270	0.0270	0.0270
$\Delta\Omega_{\rm M}$	0.020	0.0187	0.0187	0.020	0.020	0.020
$\Delta n_{\rm s}$	0.0094	0.0094	0.0094	0.0094	0.0094	0.0094
Δh	0.0140	0.0140	0.0140	0.0140	0.0140	0.0140
$\Delta f_{\rm tratio}$	0.5192	0.4608	0.4598	33.393	0.9995	0.9984
$\Delta f_{\rm Temp}$	0.0405	0.0396	0.0392	3.6606	1.9240	0.2479
$\Delta f_{\rm gas}$	0.0038	0.0035	0.0035	0.1687	0.1619	0.1404
$\Delta\alpha_{\rm gas}$	0.1052	0.0958	0.0954	4.0753	2.2890	1.7734

Additionally, for each case considered, we look at constraints for all the eight parameters listed above (equation 23) and in the second case, we repeat the same procedure but with only seven parameters, assuming that the baryonic content of galaxies is independent of redshift (i.e. $\alpha_{\rm gas} = 0$). The introduction of varying gas fraction in haloes changes the shape of C_ℓ (see, for example, in Majumdar 2001) which results in different sensitivity to the Fisher parameters; it also introduces an extra nuisance parameter to be marginalized over. The results of the first analysis (with $\alpha_{\rm gas}$ varying) are shown in Table 3 and the second case (with $\alpha_{\rm gas}$ fixed) in Table 2.

5.2 Results

We are in an era in cosmology where major surveys like *Planck* have already provided tight constraints on the parameters of the standard cosmological model. In future, two of the major goals are to go beyond the standard model of cosmology and to constrain parameters related to baryonic/gas physics associated with non-linear structures. One of the puzzles related to baryonic matter is the issue of 'missing baryons', i.e. the fact that after accounting for the gas locked up in structures (like galaxies and galaxy clusters) and the diffuse IGM, one still falls short of the cosmological mean baryon fraction $\Omega_{\rm B}$. While recently, much of this missing material may have been accounted by the ICM, a deficit of the order of at least $\sim$ tens per cent is still found.

With the growing observational evidence for CGM, it would be interesting to determine if its inclusion in the baryonic census can fill the deficit. To go forward, one needs to go beyond the discovery of the CGM in nearby isolated haloes (other than the Milky Way) or beyond what one can measure by doing a stacking analysis of gas in a sample of haloes. This is possible by probing the locked gas in and around a cosmological distribution of galaxy haloes through its signature on the CMB as shown in this paper. A constraint on the mean gas fraction, $f_{\rm gas}$, included in our calculations, provides one of the best ways to estimate the amount of circumgalactic baryons in a statistical sense. In the rest of the section, we focus on the constraints on $f_{\rm gas}$, for a variety of survey scenarios.

The constraints on the amount of baryons locked up as CGM, as well on other Fisher parameters, are shown in Tables 2 and 3. The 1σ ellipses for joint constraints of $f_{\rm gas}$ with non-cosmological parameters, for the two surveys considered and different prior choices, are shown in Figs 9, 10, 11 and 12.

5.2.1 *Constraints on CGM using kSZ + tSZ*

Strong degeneracies between the astrophysical parameters prevent us from getting any useful constraints on the CGM, using *only* cosmological priors, i.e. Prior-1, when one uses either of the tSZ or the kSZ C_ℓ alone. However, once both the tSZ and the kSZ signals are added, the strong degeneracies are broken. This is seen clearly in the upper-left panel of Fig. 9, which shows the joint constraint for the SPT-like survey. The fact that two cigar-like degeneracies, from two data sets, differing in their degeneracy directions eventually leads to very strong constraints in parameter space when taken together, is well known (see, for example, Khedekar, Majumdar & Das 2010) and the same idea is at work here. Thus, although there is practically no constraint on $f_{\rm gas}$ from using tSZ or kSZ C_ℓ from CGM individually, adding them together results in a weak constraint of $\Delta f_{\rm gas} \approx 0.11$ which is the same as the fiducial value of $f_{\rm gas}$. One of reason for this weak constraint is the additional degeneracy of $f_{\rm gas}$ with α.

This degeneracy of $f_{\rm gas}$ with α is broken either (i) when one evokes no evolution in the Fisher analysis or (ii) when additional astrophysical priors are imposed. This is shown in the upper-right and lower-left panels of Fig. 9. In both cases, the addition of astrophysical priors, for example Prior-3, can already break the strong cigar like degeneracies leaving both kSZ and tSZ signal power to constrain $f_{\rm gas}$. The difference between these two panels is that α is not fixed (i.e. we marginalize over unknown evolution) for the upper-right panel leading to slightly weaker constraints (for tSZ+kSZ) than the lower-left panel where α is held constant. The higher SNR of kSZ w.r.t tSZ (as seen in Fig. 8) gives the kSZ C_ℓ a stronger constraining power on $f_{\rm gas}$ than tSZ and the addition of tSZ C_ℓ makes only modest improvement on the constraint on CGM achieved by using kSZ C_ℓ only.

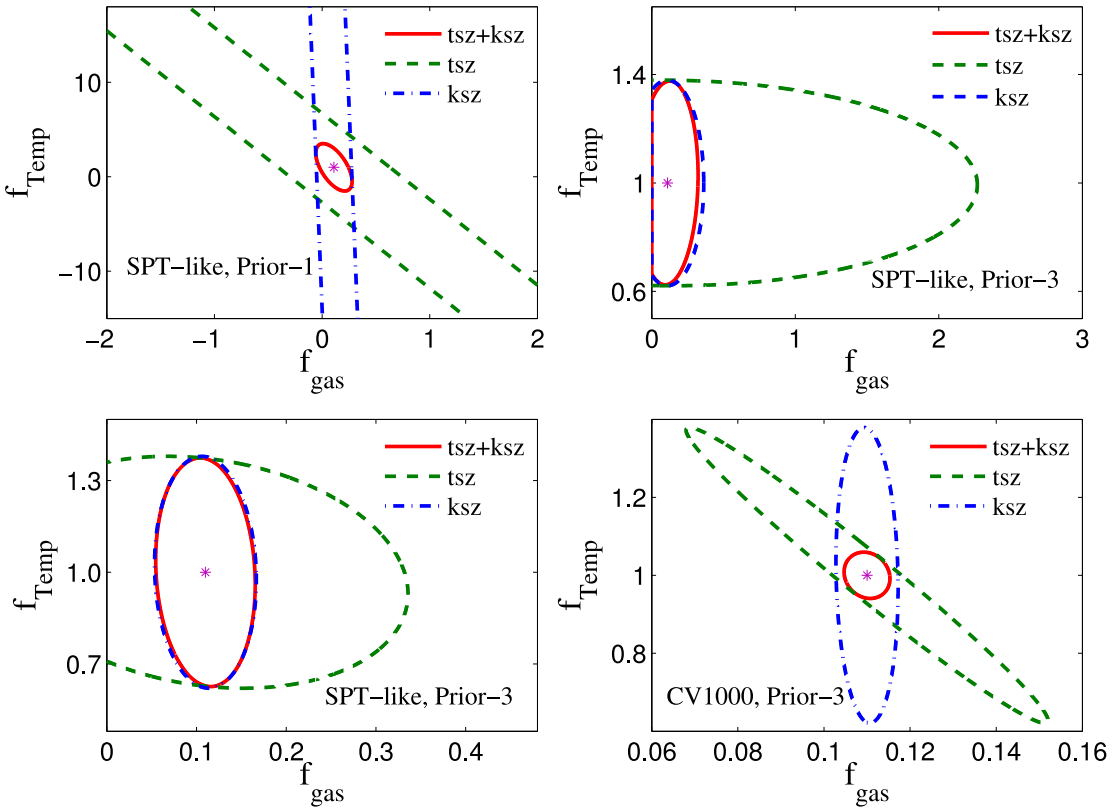

Figure 9. The figure shows the breaking of parameter degeneracy when information from tSZ C_ℓ and kSZ C_ℓ are taken together for different cases. The upper-left panel shows result from the case Prior-1, i.e. cosmological priors only, for the SPT-like survey even when α is fixed. The upper- right panel shows the case Prior-3 which includes additional priors on $f_{\rm ratio}$ and $f_{\rm Temp}$ but α, now, varied for SPT-like. The lower-left panel shows the case Prior-3 but with α fixed. The lower- right panel shows the case for CV1000 for, with Prior-3 and α varied. In all cases, green dashed line is tSZ, blue dot–dashed is kSZ and solid red line is tSZ+kSZ.

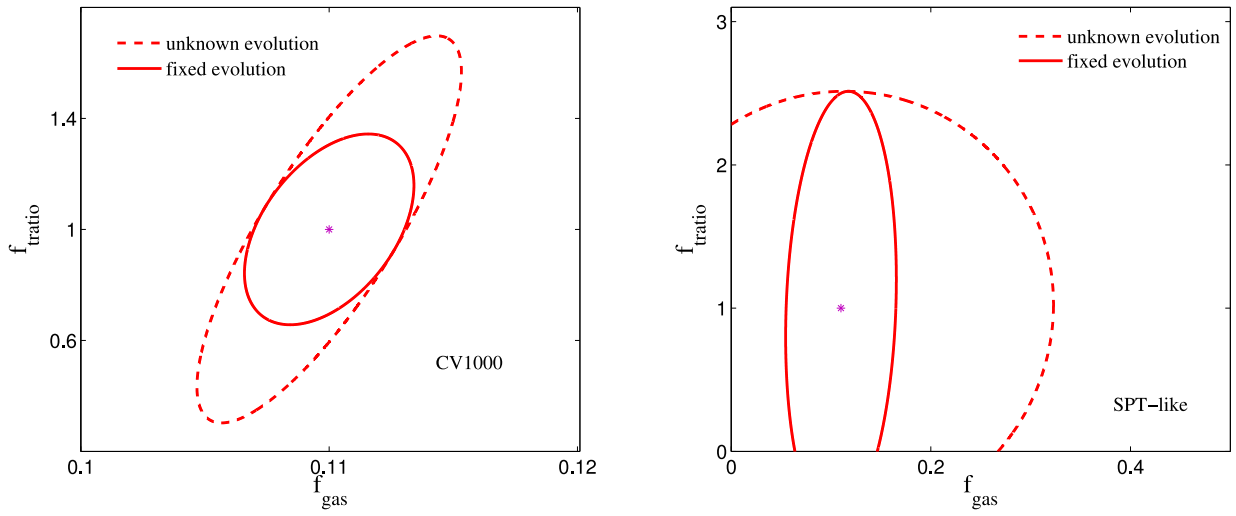

Figure 10. The figure shows that the impact on parameter constraints due to any unknown evolution of the gas fraction with redshift parametrized as $f_{\rm gas}(z) = f_{\rm gas}[E(z)]^{\alpha_{\rm gas}}$. The left-hand panel is for the survey 'CV1000' and right-hand panel is for the survey 'SPT-like'. In both cases, the red dashed line corresponds to the case of $\alpha_{\rm gas}$ is unknown and varied as one of the Fisher parameters, whereas the red solid line correspond to $\alpha_{\rm gas}$ fixed at its fiducial value.

The lower-right panel of Fig. 9 shows that constraints from the more futuristic cosmic variance limited survey CV1000 in the presence of Prior-3 but including an unknown gas fraction. In this case, due to its better sensitivity, tSZ is capable of constraining $f_{\rm gas}$ (compare green dashed ellipses in the two right-hand panels, upper and lower) and finally comes up with stronger joint constraint than SPT-like (compare the red solid ellipse in lower left and lower right). In the rest of this section, we focus mainly on constraints coming from kSZ+tSZ C_ℓ, keeping in mind that all the constraints will only be slightly degraded if only kSZ C_ℓ are used instead. Note that this is applicable as long as the astrophysical priors are added.

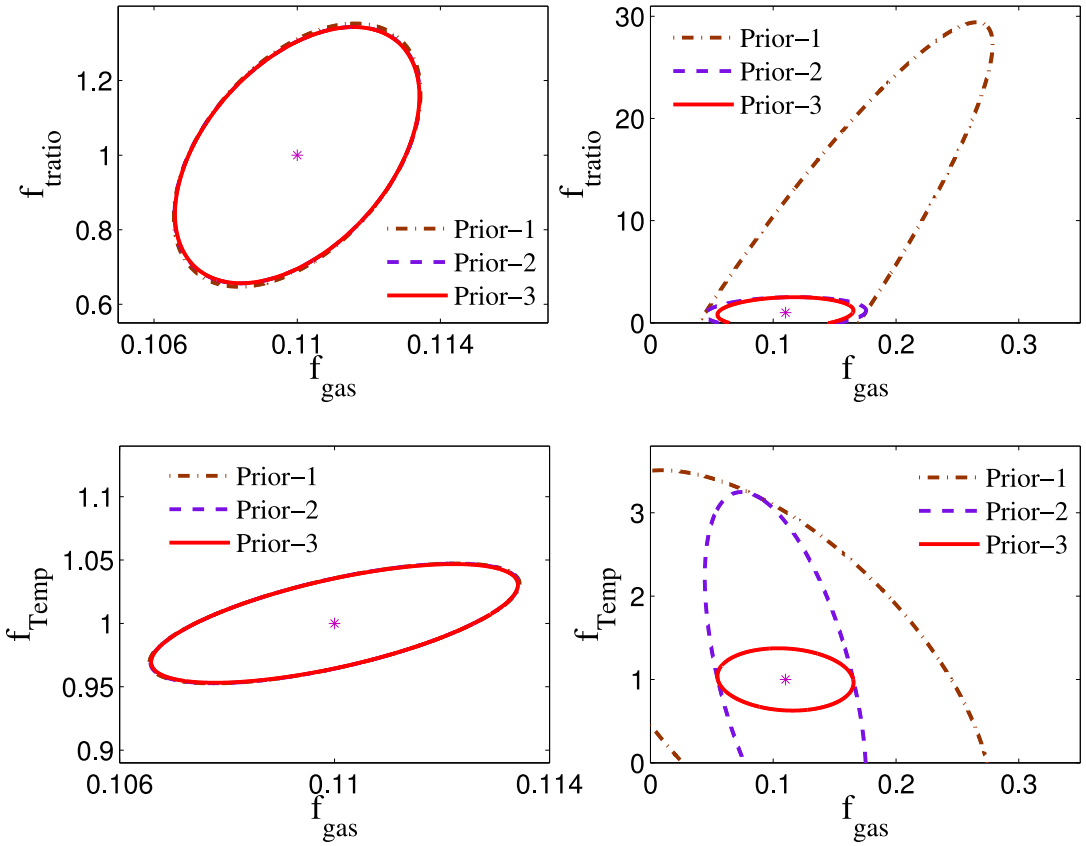

Figure 11. 1σ contours for gas physics parameters $f_{\rm gas}, f_{\rm tratio}, f_{\rm Temp}$ when $\alpha_{\rm gas}$ is fixed. The left-hand panel is for CV1000 survey and the right-hand panel is for SPT-like survey. In all cases, red solid line is Prior-3, purple dashed line is Prior-2 and brown dot–dashed line is Prior-1.

As evident above, one of the major uncertainties in our knowledge of the gas content of haloes at all scales is our lack of understanding of any redshift evolution of the gas. In using large-scale structure data to constrain cosmology, for example, an unknown redshift evolution can seriously degrade cosmological constraints (as an example, see Majumdar & Mohr 2003), and one needs to invoke novel ideas to improve constraints (Majumdar & Mohr 2004; Khedekar & Majumdar 2013). Whereas for galaxy clusters, in which case $f_{\rm gas}$ has been measured at higher redshift, and one finds evolution in gas content, no such evolution has been measured for galactic haloes considered in this work. It is however possible that feedback processes in galaxies, and cosmological infall of matter may introduce an evolution of $f_{\rm gas}$ with redshift. In order to incorporate the impact of gas evolution on our constraints, we have considered the possibility that $f_{\rm gas}$ to scales with the expansion history $E(z)$ with a power-law index α, with the fiducial value of α set to 0.

The constraints on all the parameters used in the Fisher analysis for the cases where we assume that the gas fraction to remain constant are given in Table 2. As mentioned before, in the absence of any astrophysical priors, there are no interesting constraints on $f_{\rm gas}$ (as well as $f_{\rm Temp}$ or $f_{\rm tratio}$) for SPT-like survey. However, for the CV1000 survey the amount of gas locked as CGM can be constrained very tightly to better than 2 per cent; similarly, with cosmological priors only CV1000 can constraint departure from the virial temperature to 3.1 per cent and $f_{\rm tratio}$ to $\sim$23 per cent. The addition of astrophysical priors, either Prior-2 or Prior-3 does not improve the constraints for CV1000 any further, since the constraints with Prior-1 are much tighter than the priors imposed. However, astrophysical priors considerably improve the constraints for the SPT-like survey especially for $f_{\rm gas}$ which is constrained to 39 per cent when Prior-2 is used and is further constrained to better than 33 per cent accuracy with Prior-3. This means that for both Prior-2 and Prior-3, $f_{\rm g} = 0$ can be excluded by at least 3σ with the SPT-like survey.

The corresponding constraint ellipses showing the 1σ allowed region between $f_{\rm gas}$ and either $f_{\rm Temp}$ or $f_{\rm tratio}$ are shown in Fig. 11. The left-hand panels show the degeneracy ellipses for CV1000 whereas the right-hand panels show the same for SPT-like. Notice, from the upper panels, that $f_{\rm tratio}$ has a positive correlation with $f_{\rm gas}$. This can be understood by noting that any increase in $f_{\rm gas}$ increases C_ℓ whereas it can be offset by an increase $f_{\rm tratio}$ which pushes up the lower limit of halo mass (see Fig. 1) and hence decreases the number density of haloes thus lowering the C_ℓ. The anticorrelation of $f_{\rm gas}$ with $f_{\rm Temp}$, seen in the lower-right panel, is a consequence of the anticorrelation of $n_{\rm e}$ and T_v (in equation 1) in the tSZ relation which modulates the overall degeneracy direction of tSZ+kSZ. Note that for the CV1000 survey, the 1σ ellipses are almost degenerate whereas priors shape the relative areas of the ellipses for the SPT-like survey.

A fixed non-evolving $f_{\rm gas}$, although desirable, is rather naive. Given our lack of understanding of the energetics affecting the CGM over cosmic time-scales, it is prudent to marginalize over any unknown evolution of $f_{\rm gas}$ parametrized, here, by α. The resultant constraints are given in Table 3. The presence over one extra unknown gas evolution parameter to marginalize overdilutes the constraints on $f_{\rm gas}$ for the both surveys. For the CV1000 survey (Fig. 10), the constraints are still strong and hovers around 3 per cent for all the three prior choices. Moreover, $f_{\rm Temp}$ and $f_{\rm tratio}$ can still be

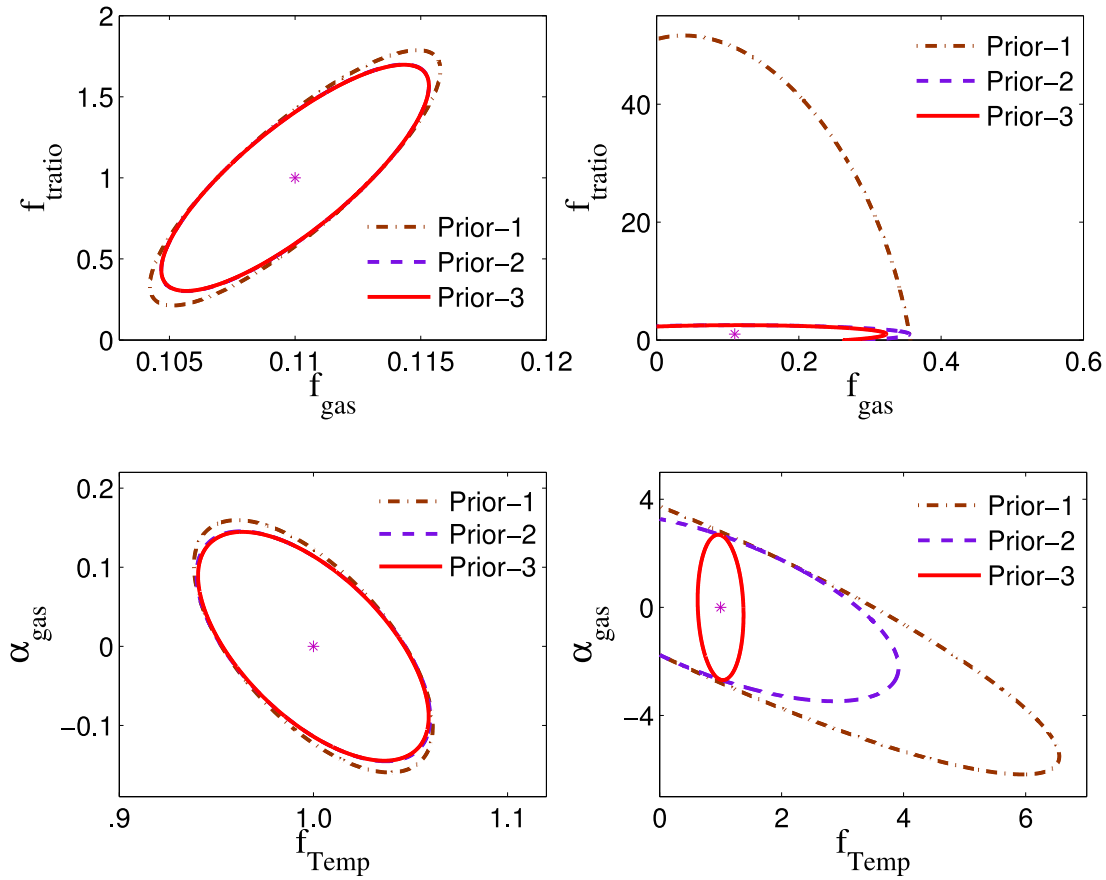

Figure 12. 1σ contours for gas physics parameters $f_{\rm gas}, f_{\rm tratio}, f_{\rm Temp}, \alpha_{\rm gas}$. The left-hand panel is for CV1000 survey and the right-hand panel is for SPT-like survey. In all cases red solid line is Prior-3, purple dashed line is Prior-2 and brown dot–dashed line is Prior-1.

constrained to ∼4 and ∼46 per cent by the futuristic survey. Without any external prior on α, all parameters poorly constrained by the SPT-like survey. With CV1000 survey, one can get a much stringent constraint on any possible evolution of the CGM with $\Delta\alpha \sim 0.1$

5.2.2 *Constraints on cosmology*

The parameters of the standard cosmological model are already tightly constrained by *Planck*. These are the constraints that are used as Prior-1 in this paper. With the SNR possible in an SPT-like survey, it is not possible to tighten the cosmological constraints further irrespective of whether we know α or it is marginalized over. However, with the larger sensitivity of CV1000 survey, it is possible to further improve cosmological parameters, albeit with α fixed. A quick look at Table 2 shows that it is possible to shrink the 1σ error on σ_8 by almost a factor of 2 and that on $\Omega_{\rm M}$ by ∼20 per cent.

5.2.3 *Constraints on the density profile of CGM*

We have so far assumed the density profile of CGM to be uniform, which was argued on basis of current observations (Putman et al. 2012; Gatto et al. 2013). However, it is perhaps more realistic to assume that the density profile to decrease at large galactocentric distances. One can ask if it would be possible to determine the pressure profile of the halo gas from SZ observations in the near future. In order to investigate this, we parametrize the density profile by $\gamma_{\rm gas}$ such that $\rho_{\rm gas}(r) \propto (1 + (\frac{r}{R_{\rm s}})^{\gamma_{\rm gas}})^{-1}$, where $R_{\rm s}$ is the scale radius defined as $R_{\rm s} \equiv R_{\rm vir}/c(M, Z)$ and $c(M, Z)$ is the concentration parameter. This density profile gives uniform density at $r << R_{\rm s}$ and $\rho_{\rm gas}(r) \propto r^{-\gamma_{\rm gas}}$ at $r \gg R_{\rm s}$. We include $\gamma_{\rm gas}$ in Fisher matrix analysis with fiducial value $\gamma_{\rm gas} = 0$. For CV1000 survey with a fixed $\alpha_{\rm gas}$ and Prior-3, the constrain on density profile of CGM is $\gamma_{\rm gas} < 1.5$ whereas the constrain degrades to $\gamma_{\rm gas} < 3.15$ in the presence of an unknown redshift evolution of gas fraction. $\gamma_{\rm gas}$ poorly constrained by SPT-like survey.

6 SZ EFFECT FROM WARM CGM

The observations of Tumlinson et al. (2011) have shown the existence of O VI absorbing clouds, at $10^{5.5}$ K, with hydrogen column density $N_{\rm H} \sim 10^{19-20}$ cm^{-2}. The integrated pressure from this component in the galactic halo is estimated as $\langle p \rangle \sim N_{\rm H} kT$. This implies a tSZ y-distortion of the order of $y_{\rm O\,VI} \sim N_{\rm H} kT \sigma_{\rm T}/(m_{\rm e}\, c^2) \sim 3.6 \times 10^{-9}\, N_{\rm H,20}$, where $N_{\rm H} = 10^{20} N_{\rm H,20}$ cm^{-2}.

There is also a cooler component of CGM, at ∼10^4 K, which is likely to be in pressure equilibrium with the warm CGM. The COS-Halos survey have shown that a substantial fraction of the CGM can be in the form of cold (∼10^4 K). Together with the warm O VI absorbing component, this phase can constitute more than half the missing baryons (Werk et al. 2014). Simulations of the interactions of galactic outflows with halo gas in Milky Way-type galaxies also show that the interaction zone suffers from various instabilities, and forms clumps of gas at 10^4 K (Marinacci et al. 2010; Sharma et al. 2014). These are possible candidates of clouds observed with

Na I or Mg II absorptions in galactic haloes. Cross-correlating Mg II absorbers with SDSS, *WISE* and *GALEX* surveys, Lan, Ménard & Zhu (2014) have concluded that some of the cold Mg II absorbers are likely associated with outflowing material. However, for similar column density of these clouds, the SZ signal would be less than that of the warm components by $10^{-1.5}$ because of the temperature factor.

We can calculate the integrated y-distortion due to the CGM in intervening galaxies, by estimating the average number of galaxies in the appropriate mass range (10^{12-13} $M_\odot$) in a typical line of sight, using Monte Carlo simulations. Dividing a randomly chosen line of sight, we divide it in redshift bins up to $z = 8$, and each redshift bin is then populated with haloes using the ST mass function, in the above mentioned mass range. We estimate the average number to be $\sim$20 after averaging over 50 realizations. This implies an integrated y-parameter of the order of $7.5 \times 10^{-8}\, N_{\rm H,20}$. This can be detected with upcoming experiments such as *Primordial Inflation Explorer* (*PIXIE*) even with $N_{\rm H} = 10^{19}$ cm^{-2}, since it aims to detect spectral distortion down to $y \geq 2 \times 10^{-9}$ (Kogut et al. 2011).

The kSZ signal from the warm gas in galactic haloes can be estimated from equation (3), writing $v_{\rm local}$ as the local (line-of-sight) velocity dispersion. Recent studies indicate that CGM gas is likely turbulent, probably driven by the gas outflows (Evoli & Ferrara 2011). If we consider transonic turbulence for this gas, then $v_{\rm los}/c \sim \sqrt{kT/m_{\rm p}c^2}$. Then we have

$$\frac{\Delta T_{\rm kin}}{\Delta T_{\rm th}} \approx \frac{1}{2}\frac{m_{\rm e}}{m_{\rm p}}\sqrt{\frac{m_{\rm p}c^2}{kT_{\rm e}}} = \frac{m_{\rm e}}{2m_{\rm p}}\frac{c}{v_{\rm loc}}\,. \tag{25}$$

For $v_{\rm loc} \sim 100$ km s^{-1} (corresponding to gas with temperature $\sim 10^6$ K), the kSZ signal from turbulent gas is, therefore, comparable to the tSZ signal.

7 CONCLUSIONS

We have calculated the SZ distortion from galactic haloes containing warm and hot circumgalactic gas. For the hot halo gas, we have calculated the angular power spectrum of the distortion caused by haloes in which the gas cooling time is longer than the halo destruction time-scale (galactic haloes in the mass range of 5×10^{11}–$10^{13}\, h^{-1}$ $M_\odot$). The SZ distortion signal is shown to be significant at small angular scales ($\ell \sim 10^4$), and larger than the signal from galaxy clusters. The kSZ signal is found to dominate over the tSZ signal for galactic haloes, and also over the tSZ signal from galaxy clusters for $\ell > 10\,000$. We also show that the estimated Comptonization parameter $\tilde{Y}_{500}$ for most massive galaxies (halo mass $\geq 10^{12.5}$ $M_\odot$) is consistent with the marginal detection by *Planck*. The integrated Compton distortion from the warm CGM is estimated to be $y \sim 10^{-8}$, within the capabilities of future experiments.

Finally, we have investigated the detectability of the SZ signal for two surveys, one which is a simple extension of the SPT survey that we call SPT-like and a more futuristic cosmic variance limited survey termed CV1000. We find that for the SPT-like survey, kSZ from CGM has an SNR of $\sim 2\sigma$ and at much higher SNR for the CV1000 survey. We do a Fisher analysis to assess the capability of these surveys to constrain the amount of CGM. Marginalizing over cosmological parameters, with *Planck* priors, and astrophysical parameters affecting the SZ C_ℓ from CGM, we find that in the absence of any redshift evolution of the gas fraction, the SPT-like survey can constrain $f_{\rm gas}$ to $\sim$33 per cent, and the CV1000 survey to $\sim$2 per cent. Solving simultaneously for an unknown evolution of the gas fraction, the resultant constraints for CV1000 becomes 3 per cent, and it is poorly constrained by SPT-like survey. We also find that a survey like CV1000 can improve cosmological errors on σ_8 obtained by *Planck* by a factor of 2, if one has knowledge of the gas evolution. The Fisher analysis tells us that if indeed $\sim$10 per cent of the halo mass is in the circumgalactic medium, then this fraction can be measured with sufficient precision and can be included in the baryonic census of our Universe.

ACKNOWLEDGEMENTS

We thank the anonymous referee for valuable suggestions and comments. PS and BN would like to thank Jasjeet Singh Bagla and Suman Bhattacharya for helpful discussions. SM acknowledges the hospitality of Institute for Astronomy at ETH-Zurich where the project was completed during the author's Sabbatical.

REFERENCES

Addison G. E., Dunkley J., Spergel D. N., 2012, MNRAS, 427, 1741
Anderson M. E., Bregman J. N., 2010, ApJ, 714, 320
Anderson M. E., Bregman J. N., 2011, ApJ, 737, 22
Anderson M. E., Bregman J. N., Dai X., 2013, ApJ, 762, 106
Anderson M. E., Gaspari M., White S. D. M., Wang M., Dai W., 2014, preprint (arXiv:1409.6965v1)
Benson A. J., Bower R. G., Frenk C. S., White S. D. M., MNRAS, 2000, 314, 557
Bhattacharya S., Kosowsky A., 2008, Phys. Rev. D, 77, 083004
Birnboim Y., Dekel A., 2003, MNRAS, 345, 349
Bogdán Á. et al., 2013a, ApJ, 772, 97
Bogdán Á., Forman W. R., Kraft R. P., Jones C., 2013b, ApJ, 772, 98
Crain R. A., McCarthy I. G., Frenk C. S., Theuns T., Schaye J., 2010, MNRAS, 407, 1403
Dai X., Anderson M. E., Bregman J. N., Miller J. M., 2012, ApJ, 755, 107
Duffy A. R., Battye R. A., Davies R. D., Moss A., Wilkinson P. N., 2008, MNRAS, 383, 150
Dutton A. A., Conroy C., vanden Bosch F. C., Prada F., More S., 2010, MNRAS, 407, 2
Efstathiou G., Migliaccio M., 2012, MNRAS, 423, 2492
Evoli C., Ferrara A., 2011, MNRAS, 413, 2721
Fang T., Bullock J., Boylan-Kolchin M., 2013, ApJ, 762, 20
Fukugita M., Hogan C. J., Peebles P. J. E., 1998, ApJ, 503, 518
Gatto A., Fraternali F., Read J. I., Marinacci F., Lux H., Walch S., 2013, MNRAS, 433, 2749
Gradshteyn I. S., Ryzhik I. M., 1980, Tables of Integrals, Series and Products. Academic Press, New York
Grcevich J., Putman M. E., 2009, ApJ, 696, 385
Hamana T., Kayo I., Yoshida N., Suto Y., Jing Y. P., 2003, MNRAS, 343, 1312
Jing Y. P., 1999, ApJ, 515, L45
Khedekar S., Majumdar S. S., 2013, J. Cosmol Astropart. Phys., 2, 30
Khedekar S., Majumdar S., Das S., 2010, Phys. Rev. D, 82, 041301
Kogut A. et al., 2011, J. Cosmol Astropart. Phys., 7, 25
Komatsu E., Kitayama T., 1999, ApJ, 526, L1
Komatsu E., Seljak U., 2002, MNRAS, 336, 1256
Lacey C., Cole S., 1993, MNRAS, 262, 627
Lacey C., Cole S., 1994, MNRAS, 271, 676
Lan T.-W., Ménard B., Zhu G., 2014, Astrophys. J., 795, 31
Leauthaud A. et al., 2012, ApJ, 744, 159
Majumdar S., 2001, ApJ, 555, L7
Majumdar S., Mohr J. J., 2003, ApJ, 585, 603
Majumdar S., Mohr J. J., 2004, ApJ, 613, 41
Maller A. H., Bullock J. S., 2004, MNRAS, 355, 694
Marinacci F., Binney J., Fraternali F., Nipoti C., Ciotti L., Londrillo P., 2010, MNRAS, 404, 1464

Mitra S., Kulkarni G., Bagla J. S., Yadav J. K., 2011, Bull. Astron. Soc. India, 39, 563
Mo H. J., Mao S., White S. D. M., 1998, MNRAS, 295, 319
Moster B. P., Maccio A. V., Somerville R. S., Johansson P. H., Naab T., 2010, MNRAS, 403, 1009
Planck Collaboration XI, 2013, A&A, 557, 52
Planck Collaboration XVI, 2014, A&A, 571, A16
Putman M. E., Peek J. E. G., Joung M. R., 2012, ARA&A, 50, 491
Rassmussen J., Sommer-Larsen J., Pedersen K., Toft S., Benson A., Bower R G., Grove L. F., 2009, ApJ, 697, 79
Sharma P., McCourt M., Parrish I. J., Quataert E., 2012, MNRAS, 427, 1219
Sharma M., Nath B. B., Chattopadhyay I., Shchekinov Y., 2014, MNRAS, 441, 431
Sheth R. K., Diaferio A., 2001, MNRAS, 322, 901
Sheth R. K., Mo H. J., Tormen G., 2001, MNRAS, 323, 1
Silk J., 1977, ApJ, 211, 638
Sutherland R. S., Dopita M. A., 1993, ApJ, 88, 253
Tumlinson J. et al., 2011, Science, 334, 948
Walker S. A., Bagchi J., Fabian A. C., 2014, preprint (arXiv:1411.1930v1)
Werk J. K. et al., 2014, Astrophys. J., 792, 8
White S. D. M., Frenk C. S., 1991, ApJ, 379, 52
White S. D. M., Rees M. J., 1978, MNRAS, 183, 341

This paper has been typeset from a TEX/LATEX file prepared by the author.